Check for updates

CATALYSIS

Dependence of catalytic properties of strongly supported platinum clusters with atom counts

Chyan Kyung Song[1,2]†, Junhyeok Jung[1,2]†, Shyama Charan Mandal[3], Sungsu Kang[1,2], Tae Yong Kim[1,4], Chan Kim[1,2,5], Gyeongrok Jang[1,2], Hyungjoo Kim[1], Younhwa Kim[1,2], Kyung Rok Lee[1,2], Ji Soo Kim[1,2], Junjie Chen[3,6], Yongmin Kim[5], Chang Won Yoon[7], Thomas F. Jaramillo[3,6], Matteo Cargnello[6], Frank Abild-Pedersen[3], Jungwon Park[1,2,8,9,10,11]*

Metal cluster structures composed of tens of atoms represent a new class of catalysts with potentially superior catalytic activity and durability compared with those of other conventional catalysts. However, controlling the number of constituent atoms in clusters and achieving high-density loading on supports remain challenging. We reduce $PtCl_4^{2-}$ with methanol to create platinum atoms forming strongly anchored platinum clusters with controlled atom counts on selected surfaces of alumina. We resolved the atomic structures of the platinum clusters and could correlate the degree of cluster-support interaction, catalytic activity, and durability with atom counts. We demonstrate the promise of this approach by developing platinum clusters that exhibit the highest catalytic performance per platinum usage reported to date for hydrogen production from the dehydrogenation of cyclic hydrocarbon hydrogen carriers.

Supported metal catalysts are conventionally synthesized with catalyst particles in sizes of several nanometers that can enhance stability, despite the loss of mass activity because the bulk atoms do not participate in surface reactions. The challenge for high-activity catalysts, such as single-atom catalysts, is avoiding agglomeration under reaction conditions. Metal clusters that consist of only tens of atoms have the potential to be highly stable and active catalysts because their geometric and energetic characteristics are distinct from those of nanoparticles (NPs) and single atoms (*1*, *2*). Such clusters expose nearly all of the constituent atoms and have sufficient surface area to accommodate reactions involving large molecules (*3*). Furthermore, their high metal-support interface-to-volume ratio prevents independent crystallization of metal atoms, which makes it possible to synthesize clusters in amorphous or disordered forms (*4*, *5*). These structures are not facile in classical catalyst synthesis, and hence advanced catalytic properties may arise (*6*–*12*). The electronic structures of supported clusters, one of the major determinants of catalytic performance, can also be controlled by manipulating interface interactions (*13*, *14*).

Despite these characteristics expected for cluster catalysts, their controlled synthesis in the typical size regime of ~1 nm is challenging (*15*, *16*). Unless finely optimized interactions between metal particles and support are achieved, the catalyst synthesis will likely result in either the formation of largely aggregated NPs or a random distribution of metal ensembles ranging in size from single atoms to NPs on the support material. Therefore, the synthesis of cluster catalysts should be at a level where the interactions between metal precursor atoms and the support are finely controlled relative to the cohesive energy of metal atoms.

There have been a few attempts to prepare clusters based on modified conventional methods widely used for NP catalysts, whereby the metal loading of a molecular precursor is controlled (*17*–*19*). However, in these processes, ligands exist and are incorporated into the synthesis process to form unexpected stable species on the support during thermal treatments (*20*, *21*), resulting in a heterogeneous distribution of metal particle sizes and their locations on different support surfaces. The heterogeneous nature of conventional catalysts prohibits understanding of the explicit catalytic activity and fully using the expected superior catalytic performances of metal clusters.

Another challenge in developing synthetic strategies for homogeneous cluster catalysts is the difficulty in characterizing their sizes and distinct structures with atomic resolution. Without such information, characterization of the synthesized catalysts relies on conventional electron microscopy to measure the size distribution along with several spectroscopic methods. However, the interaction between clusters and the support alters their structures from those anticipated in the classical crystallization in the relevant size regime. Also, cluster size information does not inform the actual distribution of constituent atoms in the clusters. Recent studies have reported that cluster catalysts with similar sizes exhibit catalytic activities with a difference of nearly an order of magnitude (*22*), which indicates a potential discrepancy between cluster size and the number of atoms.

Catalyst preparation

We introduce homogeneous Pt cluster catalysts composed of a precisely controlled number of constituent atoms and selectively localized on desired surfaces of an Al_2O_3 support. Our synthesis method exploits counterion-free metal atoms and surface-dependent metal-support bonding. Enhanced surface mobility of counterion-free metal atoms allowed them to migrate and aggregate on specific surfaces of the support where the metal-support interaction was strong (Fig. 1A). We scaled the process to a one-pot synthesis of 20-g-scale Pt/Al_2O_3 cluster catalysts (fig. S1). The specific activity of the catalyst in hydrogen production by means of dehydrogenation of cyclic hydrocarbons could be maximized, while enhancing durability, by controlling the number of atoms in Pt clusters and tuning the degree of interaction with the support.

In the synthesis, Pt-ligand complexes were converted into ligand-free Pt single atoms and clusters directly bound onto Al_2O_3, denoted as $Pt\text{-}Al_2O_3$ (Fig. 1B). The deposition of Pt on Al_2O_3 was accomplished by reacting methanol with the $PtCl_4^{2-}$ precursor in the presence of Al_2O_3. Methanol acted as a mild reducing agent (*23*–*25*) that converted the $PtCl_4^{2-}$ precursor into metallic Pt atoms. Methanol was primarily oxidized to formaldehyde (fig. S2). Wavelet transform–extended x-ray absorption fine structure (WT-EXAFS) analysis was conducted to verify ligand removal (Fig. 1B). In 0.5 wt % $Pt\text{-}Al_2O_3$, Pt–O coordination, attributed to the binding of oxygen on the Al_2O_3 surface to Pt atoms, was predominantly observed, as verified by comparison with K_2PtCl_4, Pt, and PtO_2.

During the ligand removal process of Pt on Al_2O_3, the color of the solution remained white for Pt concentrations <0.5 wt %, and a darker color was developed for Pt concentrations >0.75 wt %, which suggested the formation of NPs (fig. S3). Transmission electron microscopy (TEM) analysis confirmed the formation of distinct Pt NPs in the case

[1]School of Chemical and Biological Engineering and Institute of Chemical Processes, Seoul National University, Seoul, Republic of Korea. [2]Center for Nanoparticle Research, Institute for Basic Science (IBS), Seoul, Republic of Korea. [3]SUNCAT Center for Interface Science and Catalysis, SLAC National Accelerator Laboratory, Menlo Park, CA, USA. [4]Department of Chemical and Biological Engineering, Korea University of Technology and Education, Cheonan, Republic of Korea. [5]Center for Hydrogen and Fuel Cells, Korea Institute of Science and Technology, Seongbuk-gu, Seoul, Republic of Korea. [6]Department of Chemical Engineering and SUNCAT Center for Interface Science and Catalysis, Stanford University, Stanford, CA, USA. [7]Department of Chemical Engineering, Pohang University of Science and Technology (POSTECH), Nam-Gu, Pohang, Republic of Korea. [8]Institute of Engineering Research, College of Engineering, Seoul National University, Seoul, Republic of Korea. [9]Advanced Institute of Convergence Technology, Seoul National University, Seoul, Republic of Korea. [10]Hyundai Motor Group–Seoul National University (HMG-SNU) Joint Battery Research Center (JBRC), Seoul National University, Seoul, Republic of Korea. [11]SNU Energy Initiative, Seoul National University, Seoul, Republic of Korea. ***Corresponding author. Email: jungwonpark@snu.ac.kr** †These authors contributed equally to this work.

Downloaded from https://www.science.org at University of Bath on October 27, 2026

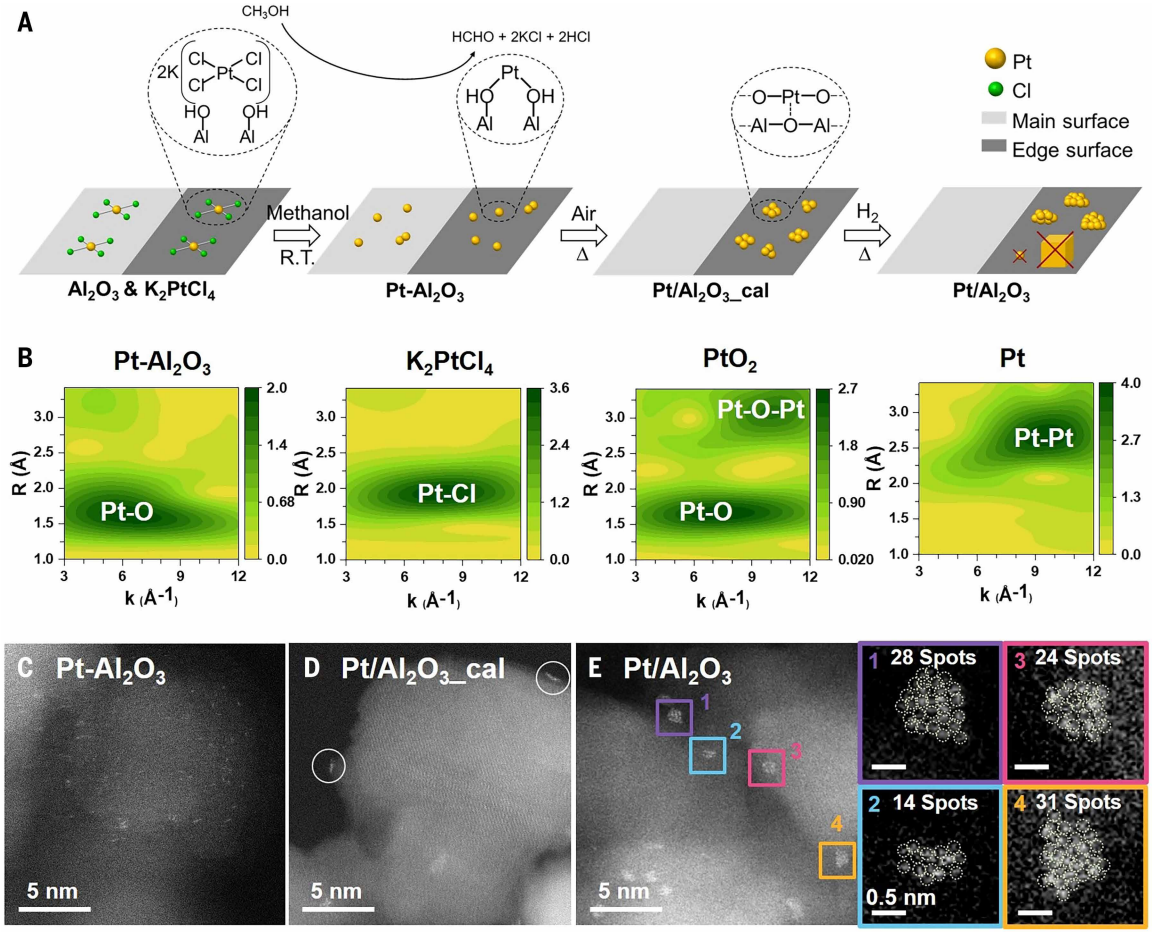


Fig. 1. Catalyst preparation process. (**A**) Schematic diagram showing the entire process of catalyst preparation. Cl^- ligands are removed from the Pt precursor by methanol and deposited on Al_2O_3 surfaces (Pt-Al_2O_3). Pt atoms are selectively deposited on the edge surface after air calcination (Pt/Al_2O_3_cal), which is a dehydrated (100) surface that interacts strongly with Pt. Pt atoms on the edge surface transform into uniform nanoclusters after hydrogen reduction (Pt/Al_2O_3). R.T., room temperature. (**B**) WT-EXAFS results of 0.5 wt % Pt-Al_2O_3, K_2PtCl_4, PtO_2, and Pt. (**C** to **E**) Aberration-corrected (Cs)–STEM images of 0.5 wt % Pt-Al_2O_3 (C); 0.5 wt % Pt/Al_2O_3_cal (D), with circles indicating induced monolayer Pt clusters on the edge surface; and 0.5 wt % Pt/Al_2O_3 (E). Four different clusters from Pt/Al_2O_3 are enlarged, and spots of distinct intensities, possibly corresponding to single Pt atoms, are indicated with dotted circles. Regions of bright contrast assigned to constituent Pt atoms in the two-dimensional STEM projections are marked by dotted circles. The number of dotted circles is indicated in each panel.

of 0.75 wt % Pt-Al_2O_3, which were not observed for 0.5 wt % Pt-Al_2O_3 (fig. S4) and below. Further investigation with atomic-resolution scanning TEM (STEM) (Fig. 1C and fig. S5) revealed the presence of Pt single atoms and clusters in 0.5 wt % Pt-Al_2O_3. This observation suggested that Pt grows into NPs beyond cluster structures when the amount of Pt present in the reaction mixture was high compared with the number of binding sites, likely hydroxyl groups, on Al_2O_3. The saturation of binding sites on Al_2O_3 was observed above 0.5 wt % of Pt deposition under the synthesis conditions used in our study (fig. S6).

An air calcination process was conducted to facilitate the surface migration of Pt atoms to settle onto the Al_2O_3 surfaces with the strongest interaction. In the system of supported Pt on Al_2O_3, PtO_x rafts exist with high stability on Al^{3+} penta-sites, primarily found on edge surfaces, such as (100) (*26*, *27*). Consistently, Pt atoms were localized on the edges of Al_2O_3 after air calcination of Pt-Al_2O_3 (Pt/Al_2O_3_cal), unlike the random distribution of Pt atoms on Al_2O_3 before air calcination (Fig. 1D and fig. S7). The charge states of Pt measured by x-ray absorption near-edge structure (XANES) analysis were the same for 0.05, 0.1, 0.25, and 0.5 wt % Pt/Al_2O_3_cal, except for 0.75 wt % Pt/Al_2O_3_cal containing metallic Pt NPs (fig. S8). However, the distribution of Pt atoms on the Al_2O_3 surface varied (fig. S9) across 0.05, 0.1, and 0.25 wt % Pt/Al_2O_3_cal, eventually forming a monolayer cluster structure at 0.5 wt % Pt/Al_2O_3_cal. Most Pt existed as single atoms in 0.05 wt % Pt loading. Increased Pt loading resulted in the formation of ensemble atoms and clusters at the monolayer level (fig. S7).

Structural characterization

Hydrogen reduction selectively activated Pt/Al_2O_3 (Fig. 1E). The Pt structures (Fig. 2, A to E) and the size distribution of Pt species (Fig. 2, F to J) in Pt/Al_2O_3 with varying Pt contents were examined by STEM. For 0.1, 0.25, and 0.5 wt % Pt/Al_2O_3, the Pt structures mainly consisted of 1-nm clusters with an amorphous structure, and there was no notable difference in the size distribution. Clusters were selectively bonded to the edge of Al_2O_3, which indicated that the Pt structures interacted with Al_2O_3 edge surfaces that likely contained the strongest binding sites. However, for 0.05 wt % Pt/Al_2O_3, larger Pt clusters were observed. We attributed particle formation to the instability of single atoms (fig. S9) and Pt structures consisting of a very small number of atoms (fig. S10) (*28*). On the basis of the surface area of Al_2O_3 (fig. S11), we summarized the relationship between Pt surface density on the

Downloaded from https://www.science.org at University of Bath on October 27, 2026

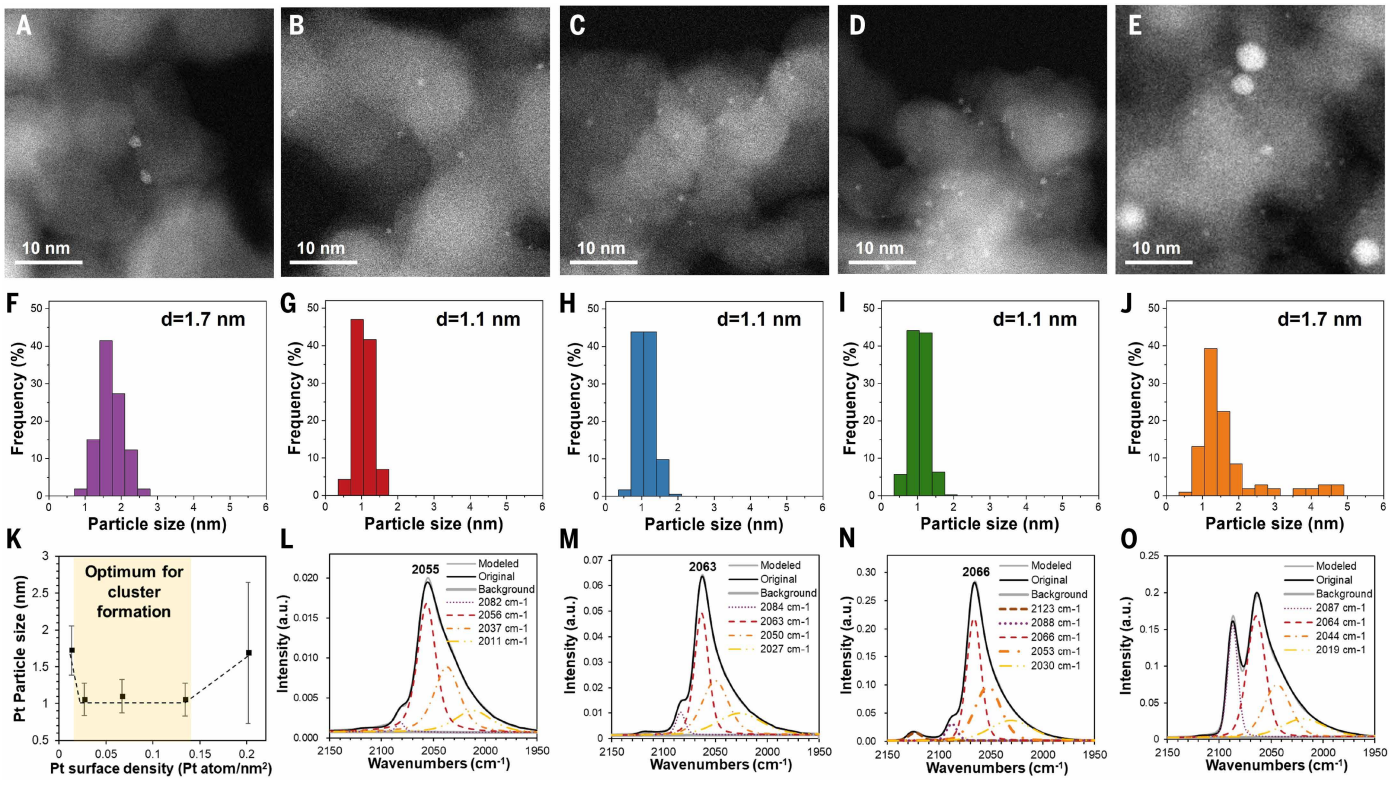


Fig. 2. Structural characterization of Pt/Al_2O_3 catalysts. (**A** to **J**) STEM images and Pt particle size distributions of 0.05 wt % [(A) and (F)], 0.1 wt % [(B) and (G)], 0.25 wt % [(C) and (H)], 0.5 wt % [(D) and (I)], and 0.75 wt % [(E) and (J)] Pt/Al_2O_3. (**K**) Pt particle sizes in Pt/Al_2O_3 catalysts depending on the Pt surface density. The size distribution of the particles is presented in the form of error bars. (**L** to **O**) CO-probe DRIFTS spectra of 0.1 wt % (L), 0.25 wt % (M), 0.5 wt % (N), and 0.75 wt % (O) Pt/Al_2O_3. a.u., arbitrary units.

support and the size of the formed Pt structures (Fig. 2K). Clusters of 1-nm size were selectively and stably synthesized on the Al_2O_3 edges when the Pt surface density was in the range of 0.027 to 0.130 Pt atoms per square nanometer of Al_2O_3.

Carbon monoxide (CO)–probe diffuse reflectance infrared Fourier transform spectroscopy (DRIFTS) analysis was conducted to characterize the surface structure of Pt clusters, which exhibited similar sizes across the range of Pt loadings studied (Fig. 2, L to O). The CO-adsorbed Pt structures were all stable for tens of minutes or longer (figs. S12 to S15). Four main bands were observed in the CO-probe DRIFTS spectrum. Recent studies of Pt cluster structures also reported four bands in CO-probe DRIFTS analysis, with lower–wave number peaks corresponding to linearly adsorbed CO on Pt atoms of lower coordination numbers (*12*). In the 0.1, 0.25, and 0.5 wt % Pt/Al_2O_3 cluster catalysts, as the Pt content decreased, the wave number of the spectral peak red shifted (fig. S16), despite the Pt clusters having similar sizes (1 nm) as measured by STEM analysis.

This result indicated that the portion of Pt atoms with low coordination numbers was high in low-content Pt/Al_2O_3 in a given range of Pt content, which implies that the structures of the clusters in those three catalysts were likely to have differences in the distribution of Pt atoms forming the clusters. We will discuss further characterization of these structures at the atomic scale below. Beyond this range of Pt content—for example, in the 0.75 wt % Pt/Al_2O_3 catalyst—the 2087 cm^{-1} band was observed, mainly corresponding to (111) terrace sites (*29*, *30*), and was consistent with Pt particles observed in STEM analysis (Fig. 2E). By contrast, for the 0.1, 0.25, and 0.5 wt % Pt cluster samples, the intensities of peaks between 2082 and 2088 cm^{-1} were low, indicating a scarcity of terrace sites and a low proportion (around 2 to 5%) of high-coordination Pt atoms (table S2).

Atomic-scale characterization of Pt clusters

We investigated the atomic structures of 1-nm Pt clusters in the 0.1, 0.25, and 0.5 wt % Pt/Al_2O_3 catalysts using high-resolution STEM (Fig. 3A). Clusters are prone to undergo restructuring by motion of constituent atoms during STEM imaging (*31*, *32*), and we therefore optimized imaging conditions for cluster catalysts. We used a focused electron beam with a flux that is slightly higher than that commonly used in conventional STEM. It enabled the 1-nm Pt cluster structures to disperse on the support material down to atomic monolayers on the support material without any Pt atomic loss (*33*–*35*). This change in structure to flatter structures allowed us to quantify the number of atoms in each cluster.

In the clusters composed of several tens of Pt atoms that formed near-trilayer structures, a few bright spots corresponding to atoms dispersed down to the bilayer level were occasionally observed, which were counted as two Pt atoms (fig. S17). The clusters in the 0.1, 0.25, and 0.5 wt % Pt/Al_2O_3 samples were similar in size and shape before beam manipulation (Fig. 3, B, F, and J). However, after beam-induced dispersion, imaging revealed that the Pt clusters were composed of different numbers of atoms (Fig. 3, C, G, and K). It further allowed for counting the number of constituent atoms in flattened monolayers, revealing the distribution of the number of atoms constituting the Pt clusters (Fig. 3, D, H, and L). The most frequently observed numbers of atoms were ~13, 25, and 31 for the 0.1, 0.25, and 0.5 wt % Pt/Al_2O_3 systems, respectively.

To understand the structures of clusters with the same in-plane dimension but with different numbers of constituent atoms, a side-view structural analysis of clusters was conducted using STEM under conditions that minimize structural deformation. The clusters in the 0.1 wt % Pt/Al_2O_3 sample are estimated to have a bilayer thickness,

Downloaded from https://www.science.org at University of Bath on October 27, 2026

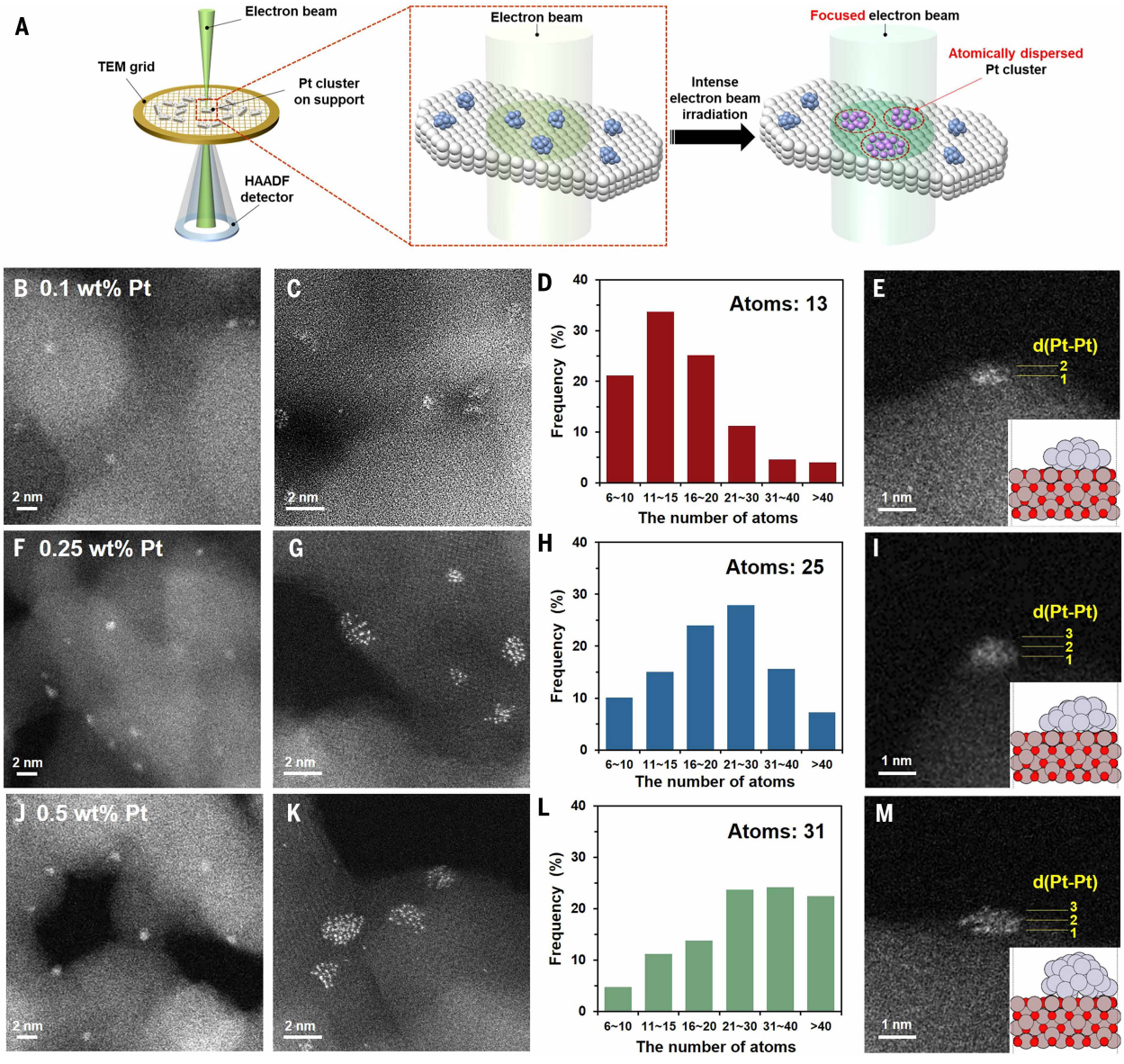


Fig. 3. Atomic-level observation of 1-nm Pt cluster catalysts. (**A**) Schematic diagram showing the Pt cluster dispersion technique for the atomic-level analysis of 1-nm Pt clusters. Previously indistinguishable nanoclusters can be resolved after atomic dispersion under focused electron beam STEM imaging conditions. (**B**, **C**, **F**, **G**, **J**, and **K**) Atomic-resolved STEM images of 0.1 wt % Pt/Al_2O_3 (top row), 0.25 wt % Pt/Al_2O_3 (middle row), and 0.5 wt % Pt/Al_2O_3 (bottom row) before dispersion [(B), (F), and (J)] and after atomic-level dispersion [(C), (G), and (K)]. (**D**, **H**, and **L**) Distributions of the number of atoms in Pt clusters. The most frequently observed number of atoms is listed. (**E**, **I**, and **M**) Side-view atomic-level STEM observations of representative Pt clusters. The yellow lines and numbers indicate the number of Pt layers, based on the atomic diameter of Pt, denoted as d(Pt-Pt). The bottom-right schemes correspond to side views of DFT-calculated Pt/Al_2O_3 structures containing Pt_{13} (E), Pt_{24} (I), and Pt_{31} (M) nanoclusters.

whereas the clusters in the 0.25 and 0.5 wt % Pt/Al_2O_3 samples exhibited a thickness corresponding to a trilayer (Fig. 3, E, I, and M). The observation that Pt structures were thinner as the Pt content decreased was further confirmed by annular bright-field (ABF)–STEM (fig. S18). Clusters composed of sufficiently thin Pt atomic layers were visible in the high-angle annular dark-field (HAADF) mode but invisible in the ABF mode, and the fraction of such ABF-invisible clusters increased with decreasing Pt loading.

The results from density functional theory (DFT) calculations showed consistent structural characteristics of the clusters as observed in STEM analysis. Structural relaxation of Pt_{13}, Pt_{24}, and Pt_{31} clusters on the Al_2O_3 surface was conducted to derive the thermodynamically favorable cluster structures in 0.1, 0.25, and 0.5 wt % Pt/Al_2O_3 (Fig. 3, E, I, and M, and fig. S19). Regardless of the initial configurations before relaxation, whether the Pt clusters were initialized as monolayer or multilayer structures (fig. S10), the optimized geometries converged to similar morphologies: Pt_{13}/Al_2O_3 formed a bilayer-like structure, whereas Pt_{24}/Al_2O_3 and Pt_{31}/Al_2O_3 adopted trilayer-like architectures, in good agreement with the side-view STEM observations. When viewed from the top, however, the stabilized Pt_{13}, Pt_{24}, and Pt_{31} clusters exhibited nearly identical lateral dimensions. The in-plane size corresponds to approximately four to five times the Pt atomic diameter (0.277 nm), yielding a projected size of 0.9 to 1.2 nm in STEM images, which matches well with the measured value of ~1.1 nm.

Investigation of the cluster-support interaction

Distinct cluster structures observed in 0.1, 0.25, and 0.5 wt % Pt/Al_2O_3 motivate examination of the electronic state and coordination environment

Downloaded from https://www.science.org at University of Bath on October 27, 2026

of Pt structures by x-ray absorption fine structure (XAFS). The Pt L3-edge XANES regions for the 0.1, 0.25, 0.5, and 0.75 wt % Pt/Al_2O_3 samples were studied (Fig. 4A). The white line for these samples was positioned between Pt foil and PtO_2. Notably, in the 0.1, 0.25, and 0.5 wt % Pt/Al_2O_3 samples, which all showed similar 1-nm cluster sizes, the white-line intensity decreased as the Pt content increased. This result suggested that Pt clusters composed of a larger number of atoms had an electronic state closer to that of Pt metal. By contrast, the 0.75 wt % Pt/Al_2O_3 sample exhibited a much lower white-line intensity compared with the other catalysts, which we attributed to the presence of NPs.

We obtained Fourier-transformed (FT)–EXAFS data to investigate the coordination environment of Pt structures and their interaction with Al_2O_3 (Fig. 4B). In the 0.1, 0.25, and 0.5 wt % Pt/Al_2O_3 catalysts, Pt–O coordination was predominantly observed, whereas Pt–Pt coordination was mainly observed in the 0.75 wt % Pt/Al_2O_3 catalyst. The 0.65 wt % Pt/Al_2O_3 sample exhibited intermediate structural features between the 0.5 and 0.75 wt % samples (fig. S20). Among the Pt cluster catalysts, 0.1 wt % Pt/Al_2O_3 showed the highest extent of Pt–O bonds, whereas 0.25 wt % Pt and 0.5 wt % Pt/Al_2O_3 exhibited a similar degree of Pt–O bonds, although slightly fewer in 0.5 wt % Pt/Al_2O_3.

This difference can be explained by the different proportions of Pt atoms directly interacting with oxygen on the Al_2O_3 surface in the three cases, depending on the number of atoms composing the cluster structure. Given that the main structure in 0.1 wt % Pt/Al_2O_3 consisted of Pt clusters of around 13 atoms and was closer to a bilayer configuration, a relatively high Pt–O coordination number was expected. In the 0.25 and 0.5 wt % Pt/Al_2O_3 samples, where Pt clusters were closer to trilayer structures and composed of 25 and 31 atoms, respectively, the Pt–O coordination number was lower compared with 0.1 wt % Pt/Al_2O_3. Pt–Pt coordination was not observed in any of the cluster catalysts, consistent with previous observations in other supported cluster studies (*22*, *36*). This generally suggests that the structures may remain in a PtO_x state even after reduction treatment, or it could be attributed to a disorder effect of metal-metal coordination within cluster structures (*37*). In our study, the flattening of clusters because of strong cluster-support interactions might further contribute to the lack of Pt–Pt coordination.

In addition to Pt–O coordination, additional types of coordination are evident in the 0.1, 0.25, and 0.5 wt % Pt/Al_2O_3 samples (Fig. 4C), presumably associated with a strong interface interaction with the ligand-free uniform cluster catalysts. To identify the element in Al_2O_3 responsible for the observed coordination at 2.1 Å, fitting was performed on the 0.5 wt % Pt/Al_2O_3 sample (Fig. 4, D and E) using DFT-derived models of strongly interacting $Pt\text{-}Al_2O_3$ structures. These models include $Pt\text{–}Al_{penta}$ coordination, which exists adjacent to the Pt–O bonding (fig. S21). The FT-EXAFS spectrum of 0.5 wt % Pt/Al_2O_3 was successfully fitted using Pt–O and $Pt\text{–}Al_{penta}$ coordination (Fig. 4D). By contrast, adding a second artificial Pt–O coordination led to a poor fit (Fig. 4E). This result confirmed the presence of $Pt\text{–}Al_{penta}$ coordination, representing a strong interaction between Pt and Al_2O_3 in the 0.5 wt % Pt/Al_2O_3 sample (table S3).

It was challenging to reliably observe $Pt\text{–}Al_{penta}$ coordination through fitting in the 0.25 and 0.1 wt % Pt/Al_2O_3 samples, possibly because of its small contribution compared with Pt–O coordination. Therefore, WT-EXAFS analysis was performed to confirm the presence of $Pt\text{–}Al_{penta}$ coordination (Fig. 4, F to K). For the 0.1, 0.25, and 0.5 wt % Pt/Al_2O_3 cluster catalysts, $Pt\text{–}Al_{penta}$ coordination was observed around radial distance (R) = 2.15 Å and wave number (k) = 6.5 $Å^{-1}$. The intensity increased as the number of atoms in the clusters increased, indicating more effective interaction with Al_2O_3. This coordination was not observed in 0.75 wt % Pt/Al_2O_3, Pt foil, and PtO_2. Because metal NPs were formed above a 0.5 wt % Pt concentration and were composed of several hundreds to thousands of atoms—tens to hundreds of times as many atoms as in the clusters—the 0.75 wt % Pt catalyst exhibited only Pt–Pt contributions, which was a typical characteristic of metallic Pt.

WT-EXAFS analysis additionally revealed the presence of Pt–O–Al coordination around 3 Å in the three-cluster catalysts, serving as another indicator of strong interface interaction (Fig. 4, L to Q). The contribution of Pt–O–Pt in PtO_2 was observed around k = 9.5 $Å^{-1}$,

Downloaded from https://www.science.org at University of Bath on October 27, 2026

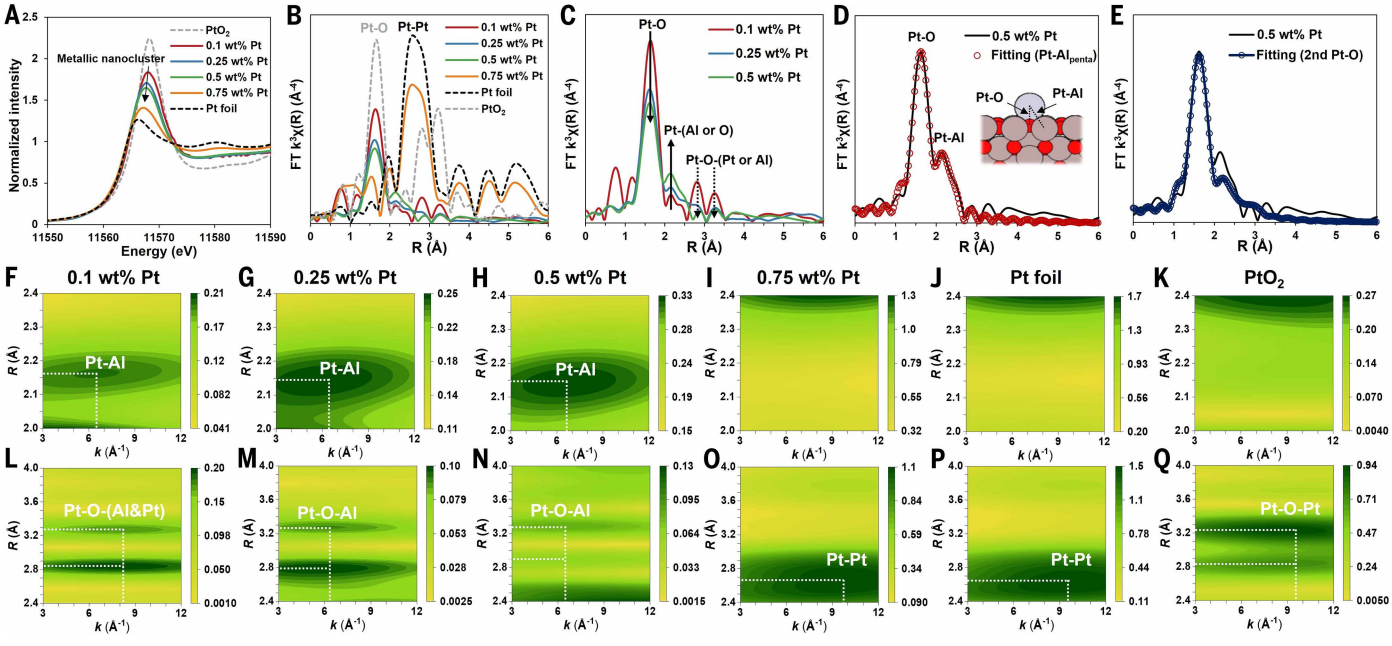


Fig. 4. Electronic state and coordination structures of Pt/Al_2O_3 catalysts. (**A** and **B**) Pt L3-edge XANES (A) and k^3-weighted FT-EXAFS (B) analysis results of Pt/Al_2O_3, Pt foil, and PtO_2. (**C**) k^3-weighted FT-EXAFS spectra of 0.1 wt % Pt, 0.25 wt % Pt, and 0.5 wt % Pt/Al_2O_3 catalysts, clearly presenting the two additional coordination environments beyond Pt–O. (**D** and **E**) Fitting results of the 0.5 wt % Pt/Al_2O_3 FT-EXAFS spectrum using DFT-derived $Pt\text{–}Al_{penta}$ coordination adjacent to the Pt–O bonding (D) and an arbitrary second Pt–O coordination (E). (**F** to **Q**) WT-EXAFS results of 0.1 wt % Pt [(F) and (L)], 0.25 wt % Pt [(G) and (M)], 0.5 wt % Pt [(H) and (N)], 0.75 wt % Pt/Al_2O_3 [(I) and (O)], Pt foil [(J) and (P)], and PtO_2 [(K) and (Q)].

whereas this contribution appeared around $k = 8.5$, 6.5, and 6.5 Å^{-1} for 0.1, 0.25, and 0.5 wt % Pt/Al_2O_3 samples, respectively. In WT-EXAFS data, coordination with lighter elements tended to exhibit lower k values, which allows for distinguishing the element-based coordination present (*38*, *39*). In the analysis of Pt–Al_{penta} using WT-EXAFS, we confirmed that coordination involving the Al element predominantly forms around $k = 6.5$ Å^{-1}. Thus, the coordination observed near 3 Å in the 0.25 and 0.5 wt % Pt/Al_2O_3 samples was mainly from Pt–O–Al, likely resulting from the strong interaction between the Pt cluster and Al_2O_3. On the other hand, in the 0.1 wt % Pt/Al_2O_3 sample, a mixture of Pt–O–Pt and Pt–O–Al coordination may exist, possibly because of weaker interactions between the smaller Pt clusters and the Al_2O_3 surface.

Catalytic evaluation

We anticipated that the synthesized cluster Pt catalysts would demonstrate high efficiency in reactions involving large molecules because of the distinctive structures of the cluster catalysts, characterized by disordered Pt configurations and robust interactions with the Al_2O_3 support. Hydrogen production from the dehydrogenation of cyclic hydrocarbons, such as methylcyclohexane (MCH), is widely studied as a hydrogen storage approach (*40*) and was used as a model system (Fig. 5A). Conventional heterogeneous catalysts based on metal NPs, primarily exposing (111) facets, exhibit low activity and selectivity in this reaction. We observed that cluster catalysts (0.1, 0.25, and 0.5 wt % Pt/Al_2O_3) show superior hydrogen production performance and durability compared with the 0.75 wt % Pt/Al_2O_3 catalyst.

Within the three-cluster catalysts, hydrogen production performance was enhanced by retarded deactivation as the Pt content increased. This result confirmed that cluster structures effectively facilitated the hydrogen production reaction compared with NPs. The challenge in the dehydrogenation of MCH is coke formation induced by strong adsorption of toluene, which is commonly observed in conventional

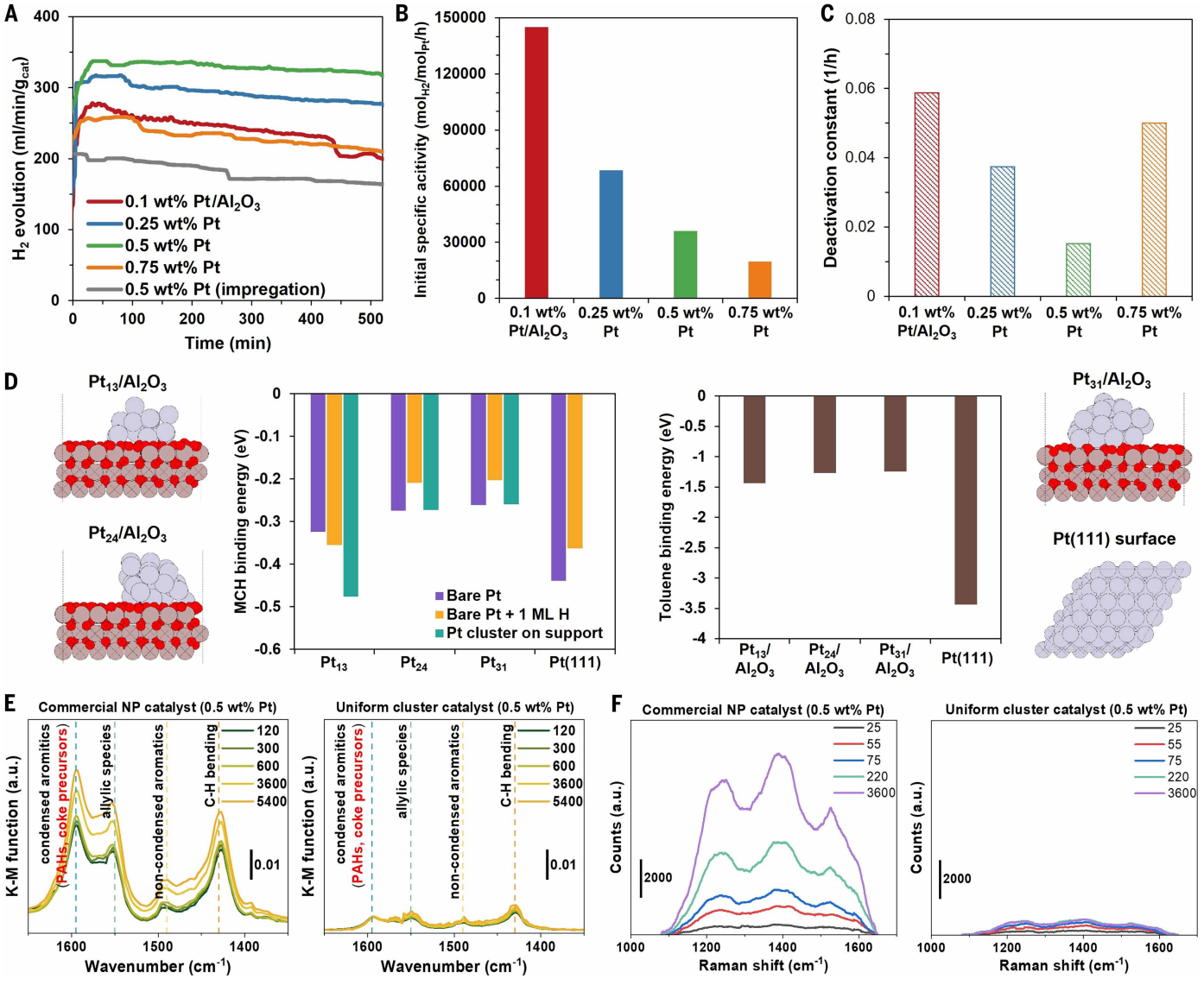


Fig. 5. Hydrogen production activity measurement. (**A** to **C**) Hydrogen evolution measurements using Pt/Al_2O_3 catalysts during MCH dehydrogenation at 300°C (A), initial specific activity (B), and deactivation constant of the Pt/Al_2O_3 catalysts (C). (**D**) Side views of the optimized Pt_{13}/Al_2O_3, Pt_{24}/Al_2O_3, and Pt_{31}/Al_2O_3 catalysts, along with the top view of a 5 × 5 Pt(111) surface. The calculated MCH binding energies are plotted for bare Pt_{13}, Pt_{24}, and Pt_{31} clusters; $Pt_{13}H_{13}$, $Pt_{24}H_{24}$, and $Pt_{31}H_{31}$ clusters with 1 monolayer (ML) hydrogen coverage; Pt_{13}/Al_2O_3, Pt_{24}/Al_2O_3, and Pt_{31}/Al_2O_3 catalysts; and both clean and hydrogen-covered Pt(111) surfaces. The calculated toluene binding energies are shown for Pt_{13}/Al_2O_3, Pt_{24}/Al_2O_3, and Pt_{31}/Al_2O_3 catalysts and for the Pt(111) surface. (**E** and **F**) In situ DRIFTS (E) and in situ Raman spectra (F) of the 0.5 wt % Pt/Al_2O_3 cluster catalyst and the 0.5 wt % Pt/Al_2O_3 commercial NP catalyst during MCH dehydrogenation, tracking coke formation. The units of the numbers in the legends are seconds.

Downloaded from https://www.science.org at University of Bath on October 27, 2026

NP catalysts as a prevailing source of catalyst deactivation (*10*, *41*). We found that the hydrogen production activity of the cluster catalysts was independent of hydrogen partial pressure because toluene appeared to be weakly adsorbed on these noncrystalline surfaces (fig. S22).

The catalytic performance of the atomically controlled 1-nm Pt cluster structures was analyzed by calculating the initial specific activity (Fig. 5B). Among the cluster catalysts, those with fewer atoms exhibited enhanced initial specific activity. We attributed this to the higher ratio of surface atoms in the cluster formed with fewer atoms, even though they have similar overall sizes. Clusters with fewer atoms were likely more ductile (*42*, *43*) while driving catalytic reaction because of their relative energetic instability, as reported in previous studies. Such enhanced ductility could be beneficial for their activity, as confirmed by the enhanced conversion rates of cluster catalysts with fewer atoms. Additionally, the cluster with fewer atoms exhibits lower apparent activation energy (fig. S23). It is likely that most surface Pt atoms in the clusters are reduced to a metallic state, whereas Pt atoms bound to Al_2O_3 remain in a $Pt^{\delta+}$ state at the operating temperature of 300°C (*44*–*46*).

When comparing the durability of cluster catalysts, deactivation occurred more rapidly in the cluster catalyst with fewer atoms (Fig. 5C). The 0.1 wt % Pt/Al_2O_3 catalyst exhibited a deactivation constant similar to that of the 0.75 wt % Pt/Al_2O_3 catalyst, and the 0.5 wt % Pt/Al_2O_3 catalyst demonstrated the highest durability. As previously discussed, Pt clusters with a higher number of atoms were bound more strongly to the Al_2O_3 surface. This stronger binding, confirmed by the Pt–Al feature, influenced catalyst stability. Hydrogen production proceeded with a selectivity of >99.9% at temperatures <340°C (fig. S24) for the 0.1, 0.25, and 0.5 wt % Pt/Al_2O_3 cluster catalysts. It is generally accepted that the deactivation predominantly occurs through coke formation at lower selectivity. However, for the cluster catalysts, nuclear magnetic resonance and gas chromatography–mass spectrometry analyses of products obtained from reactions at 300°C did not detect benzene, which is a major by-product (figs. S25 and S26). Real-time reaction analysis at various temperatures indicated that benzene only began to appear at temperatures >340°C (fig. S27).

Postreaction STEM analysis confirmed the structural stability of the cluster catalysts under hydrogen production conditions (fig. S28). For all three cluster catalysts, 0.1, 0.25, and 0.5 wt % Pt/Al_2O_3, the average size remained ~1.1 nm after reaction, and the size distributions showed no substantial differences. Nonselective carbon deposition was not observed. We therefore conducted atom-count analysis to understand the presence and origin of subtle population shifts in the atom-count distributions. We infer that Pt clusters with relatively large atom counts remain stable because of strong binding to Al_2O_3, whereas a small fraction of low-atom-count Pt clusters may undergo partial restructuring and could contribute to the formation of clusters with higher atom counts.

We investigated Pt_{13}, Pt_{24}, and Pt_{31} clusters for the reaction using DFT calculations. Because MCH and toluene adsorption affected the reaction energetics, we first computed the MCH binding energies on these clusters. As the atom count increased, MCH binding became weaker: −0.31 eV (Pt_{13}), −0.27 eV (Pt_{24}), and −0.26 eV (Pt_{31}) (Fig. 5D). This decrease may be attributed to the presence of unsaturated Pt sites in Pt_{13}, which interact more strongly with the axial C–H bond of MCH compared with the larger clusters. Hence, the binding energy trend suggests that Pt_{13} exhibited the highest catalytic activity, corresponding to the 0.1 wt % Pt/Al_2O_3 catalyst, followed by Pt_{24} and Pt_{31}.

To assess the impact of hydrogen coverage, we performed calculations on a Pt(111) surface at various hydrogen coverages. The results suggested that under reaction conditions, hydrogen forms a 1.0 monolayer coverage on the surface (fig. S29). We further evaluated MCH binding on hydrogen-covered Pt_{13}, Pt_{24}, and Pt_{31} clusters ($Pt_{13}H_{13}$, $Pt_{24}H_{24}$, and $Pt_{31}H_{31}$). The binding energies showed a similar trend, −0.36 eV ($Pt_{13}H_{13}$), −0.21 eV ($Pt_{24}H_{24}$), and −0.20 eV ($Pt_{31}H_{31}$), which indicates that hydrogen coverage did not change the relative activity trend. We considered the clusters on the Al_2O_3 (100) surface to account for the effect of support, and the MCH binding energies were −0.47 eV (Pt_{13}/Al_2O_3), −0.27 eV (Pt_{24}/Al_2O_3), and −0.26 eV (Pt_{31}/Al_2O_3), reinforcing the same trend. We also calculated binding energies of toluene on Pt(111) and the supported clusters. Toluene showed the strongest binding on Pt(111) (−3.44 eV) because of π-metal interactions on the flat surface, whereas weaker binding was observed on the disordered clusters: −1.44 eV, −1.27 eV, and −1.25 eV for Pt_{13}, Pt_{24}, and Pt_{31}/Al_2O_3, respectively. This weaker binding facilitated desorption and may explain the higher durability and selectivity of Pt_{31}/Al_2O_3, which corresponds to the 0.5 wt % Pt/Al_2O_3 catalyst.

We examined the coke-suppression mechanism associated with the disordered cluster catalyst through comparative in situ characterization of the 0.5 wt % Pt/Al_2O_3 cluster and commercial NP catalysts (fig. S30). The evolution and accumulation of coke during MCH dehydrogenation were analyzed using in situ DRIFTS (Fig. 5E and fig. S31) (*47*–*51*). The NP catalyst exhibited continuous coke accumulation over time, but the cluster catalyst showed only a small amount of coke formation at 120 s, after which almost no further deposition occurred. A combined analysis of peaks corresponding to condensed aromatics (~1595 cm^{-1}) and noncondensed aromatics (~1490 cm^{-1}) revealed distinct reactivities. The intensity of the 1595 cm^{-1} peak continuously increased for the NP catalyst, whereas it remained nearly unchanged for the cluster catalyst, with only a slight increase in the noncondensed aromatic region.

These results indicate that the coke formed on the cluster catalyst was softer and more disordered in nature. Similar trends were also observed in in situ Raman analysis (Fig. 5F and fig. S32) (*52*). In the NP catalyst, coke formation continuously progressed with reaction time, whereas in the cluster catalyst, further coke formation was almost completely suppressed after 220 s. When the coke formation rate was derived from the Raman signal (fig. S33), both the NP and cluster catalysts initially exhibited a rapid increase in coke formation followed by a gradual slowdown. However, after 3600 s, continuous coke growth was still observed for the NP catalyst, whereas the amount of coke formed on the cluster catalyst became nearly negligible. An analysis of coke disorder revealed that both catalysts showed a rapid increase and a subsequent decrease in disorder during the initial stage of coke formation (fig. S34). Nevertheless, the coke generated on the cluster catalyst remained more disordered throughout the entire process, suggesting that such soft, disordered coke may allow the reactant to remain accessible to active sites even after partial coke formation.

Furthermore, we compared the hydrogen production per unit Pt atom with previously reported systems to assess the economic viability of the cluster catalysts (fig. S35). We confirmed that the 0.1, 0.25, and 0.5 wt % Pt/Al_2O_3 catalysts achieve hydrogen production rates ranging from 3000 to 12,000 mmol H_2 per gram of Pt per minute at 300°C. This range is above the hydrogen production rates reported to date (289 to 3402 mmol H_2 per gram of Pt per minute) and is even higher than the rates reported at a reaction temperature of 350°C. Although the 0.1 wt % Pt/Al_2O_3 catalyst demonstrates the highest economic efficiency, the 0.5 wt % Pt/Al_2O_3 catalyst appeared more promising for long-term operation. To compare the catalytic performance under realistic operating conditions, the 0.5 wt % Pt/Al_2O_3 catalyst, which also falls within the standard industrial Pt loading range (*53*, *54*), was tested for MCH dehydrogenation at 340°C, and the corresponding conversion and H_2 evolution were evaluated (fig. S36). In commercial processes, liquid hourly space velocity (LHSV) values of 1 to 3 $hours^{-1}$ are typically used to achieve conversion levels of >95% (*40*, *55*). Notably, even at an LHSV of 40 $hours^{-1}$, the 0.5 wt % Pt/Al_2O_3 catalyst maintained a conversion level of >99%, potentially reducing the required catalyst loading by nearly an order of magnitude. When the conversion was ~40%—comparable to that used in recent record-setting reports (*3*, *56*)—0.5 wt % Pt/Al_2O_3 achieved an H_2 production rate of 50,285 mmol H_2 per gram of Pt per minute. The 0.5 wt % Pt/Al_2O_3 cluster catalyst shows higher hydrogen production activity and durability for more than 100 hours of reaction compared with the Pt/Al_2O_3

Downloaded from https://www.science.org at University of Bath on October 27, 2026

commercial catalyst containing 10 times as much Pt (fig. S37). Furthermore, we projected that the 0.5 wt % Pt/Al_2O_3 cluster catalyst would retain more than 90% of its initial activity for >2000 hours at LHSV values of 9 and 10 $hours^{-1}$ at 340° and 300°C, respectively (fig. S38).

Discussion

We selectively formed uniform Pt clusters that strongly interacted with specific sites on the Al_2O_3 support by removing ligands and depositing metal atoms onto the support surface. We hypothesize that Pt clusters, which appeared to be of similar size based on TEM, could consist of atom numbers that vary by more than a factor of three. Furthermore, we analyzed the variation in interactions between the support and the clusters, depending on the number of atoms in the clusters, confirming that clusters with more atoms could interact more strongly with the Al_2O_3 support.

Hydrogen production reactions by means of dehydrogenation of MCH, a representative hydrogen carrier, were achieved using Pt cluster catalysts with different atomic configurations. The catalytic performance of these clusters demonstrated one of the highest activities reported to date, with reaction rates four to five times as large as those of previously reported state-of-the-art catalysts. Smaller clusters demonstrated fast hydrogen production based on high surface atom utilization and structural flexibility, whereas larger clusters exhibited good catalytic activity along with strong Pt-Al_2O_3 interactions, contributing to higher catalyst durability. Our study highlights that, where cluster catalysts serve as optimal structures, the properties of size-optimized cluster catalysts can be substantially enhanced by adjusting the number of constituent atoms and their interactions with the support.

REFERENCES AND NOTES

1. M. Boronat, A. Leyva-Pérez, A. Corma, *Acc. Chem. Res.* **47**, 834–844 (2014).
2. K. Taylor, C. Pettiette-Hall, O. Cheshnovsky, R. Smalley, *J. Chem. Phys.* **96**, 3319–3329 (1992).
3. L. Chen *et al.*, *Nat. Commun.* **13**, 1092 (2022).
4. L. Li *et al.*, *J. Am. Chem. Soc.* **135**, 13062–13072 (2013).
5. Y. Sun, L. Zhuang, J. Lu, X. Hong, P. Liu, *J. Am. Chem. Soc.* **129**, 15465–15467 (2007).
6. K. Cheng *et al.*, *Science* **377**, 204–208 (2022).
7. S. Yao *et al.*, *Science* **357**, 389–393 (2017).
8. Z. Xu *et al.*, *Nature* **372**, 346–348 (1994).
9. M. Turner *et al.*, *Nature* **454**, 981–983 (2008).
10. Y. Deng *et al.*, *J. Am. Chem. Soc.* **144**, 3535–3542 (2022).
11. Y. Jo, D. Kim, T. W. Kim, D. Yoon, Y.-W. Suh, *Appl. Catal. B* **334**, 122848 (2023).
12. A. Sangnier *et al.*, *ACS Catal.* **11**, 13280–13293 (2021).
13. Y. Lykhach *et al.*, *Nat. Mater.* **15**, 284–288 (2016).
14. M. S. Chen, D. W. Goodman, *Science* **306**, 252–255 (2004).
15. A. Wong, Q. Liu, S. Griffin, A. Nicholls, J. R. Regalbuto, *Science* **358**, 1427–1430 (2017).
16. K. Ding *et al.*, *Science* **362**, 560–564 (2018).
17. M. Komiyama, *Catal. Rev. Sci. Eng.* **27**, 341–372 (1985).
18. J. R. Regalbuto *in Catalyst Preparation: Science and Engineering*, J. R. Regalbuto, Ed. (CRC Press, 2007), pp. 297–318.
19. L. DeRita *et al.*, *J. Am. Chem. Soc.* **139**, 14150–14165 (2017).
20. H. Lieske, G. Lietz, H. Spindler, J. Völter, *J. Catal.* **81**, 8–16 (1983).
21. C. Contescu, D. Macovei, C. Craiu, C. Teodorescu, J. A. Schwarz, *Langmuir* **11**, 2031–2040 (1995).
22. M. Macino *et al.*, *Nat. Catal.* **2**, 873–881 (2019).
23. Q.-L. Zhu, N. Tsumori, Q. Xu, *J. Am. Chem. Soc.* **137**, 11743–11748 (2015).
24. S. Chen *et al.*, *Nano Lett.* **15**, 5961–5968 (2015).
25. L. Colombi Ciacchi, W. Pompe, A. De Vita, *J. Am. Chem. Soc.* **123**, 7371–7380 (2001).
26. L. Shi *et al.*, *Angew. Chem. Int. Ed.* **54**, 13994–13998 (2015).
27. J. H. Kwak *et al.*, *Science* **325**, 1670–1673 (2009).
28. C. Dessal *et al.*, *Nanoscale* **11**, 6897–6904 (2019).
29. T. Avanesian *et al.*, *J. Am. Chem. Soc.* **139**, 4551–4558 (2017).
30. M. J. Kale, P. Christopher, *ACS Catal.* **6**, 5599–5609 (2016).
31. Z. Zhang *et al.*, *Nat. Commun.* **8**, 16100 (2017).
32. A. Corma *et al.*, *Nat. Chem.* **5**, 775–781 (2013).
33. R. Nakamura, M. Ishimaru, H. Yasuda, H. Nakajima, *J. Appl. Phys.* **113**, 064312 (2013).
34. C. H. Sherman, L. F. Lowe, E. A. Burke, *Phys. Rev.* **145**, 568–575 (1966).
35. J. G. Smith *et al.*, *Sci. Adv.* **10**, eadi0175 (2024).
36. Y. Zhao *et al.*, *Nat. Commun.* **13**, 2430 (2022).
37. S. Yamazoe *et al.*, *Nat. Commun.* **7**, 10414 (2016).
38. H. Funke, A. C. Scheinost, M. Chukalina, *Phys. Rev. B* **71**, 094110 (2005).
39. J. Timoshenko, A. Kuzmin, *Comput. Phys. Commun.* **180**, 920–925 (2009).
40. Y. Okada, E. Sasaki, E. Watanabe, S. Hyodo, H. Nishijima, *Int. J. Hydrogen Energy* **31**, 1348–1356 (2006).
41. R. Herz, W. Gillespie, E. Petersen, G. Somorjai, *J. Catal.* **67**, 371–386 (1981).
42. E. Vottero *et al.*, *ACS Catal.* **12**, 5979–5989 (2022).
43. W. Zhao, C. Chizallet, P. Sautet, P. Raybaud, *J. Catal.* **370**, 118–129 (2019).
44. W. Huang *et al.*, *Nano Lett.* **8**, 2027–2034 (2008).
45. F. Bernardi, M. C. Alves, J. Morais, *J. Phys. Chem. C* **114**, 21434–21438 (2010).
46. J. Lee, E. J. Jang, D. G. Oh, J. Szanyi, J. H. Kwak, *J. Catal.* **385**, 204–212 (2020).
47. K. Gołąbek, K. A. Tarach, K. Góra-Marek, *Dalton Trans.* **46**, 9934–9950 (2017).
48. K. Matsushita, A. Hauser, A. Marafi, R. Koide, A. Stanislaus, *Fuel* **83**, 1031–1038 (2004).
49. E.-R. On *et al.*, *ACS Catal.* **15**, 5531–5545 (2025).
50. K. Pyra, K. A. Tarach, K. Góra-Marek, *Appl. Catal. B* **297**, 120408 (2021).
51. S. Shao, H. Zhang, R. Xiao, X. Li, Y. Cai, *Fuel Process. Technol.* **178**, 88–97 (2018).
52. A. Sadezky, H. Muckenhuber, H. Grothe, R. Niessner, U. Pöschl, *Carbon* **43**, 1731–1742 (2005).
53. Y. Sekine, T. Higo, *Top. Catal.* **64**, 470–480 (2021).
54. D. Acharya, D. Ng, Z. Xie, *Membranes* **11**, 955 (2021).
55. V. Sage *et al.*, *Int. J. Hydrogen Energy* **56**, 1419–1434 (2024).
56. Z. He *et al.*, *Nat. Commun.* **16**, 92 (2025).
57. C. K. Song *et al.*, Source data for "Dependence of catalytic properties of strongly supported platinum clusters with atom counts," Zenodo (2026). https://doi.org/10.5281/zenodo.18626897.

ACKNOWLEDGMENTS

Funding: This work was supported by NRF grants funded by the Korean government [Ministry of Science and ICT (MSIT)], RS-2024-00421181 (J.P. , C.W.Y., T.F.J., and M.C.), RS-2024-00449965, and RS-2024-00467226 (J.P.); the Industrial Technology Innovation Program funded by the Ministry of Trade, Industry and Energy (MOTIE), Korea, RS-2024-00435423 (J.P.); the Hyundai Motor Company (J.P.); the US Department of Energy (DOE), Office of Science, Office of Basic Energy Sciences, Chemical Sciences, Geosciences, and Biosciences Division, Catalysis Science Program to the SUNCAT Center for Interface Science and Catalysis (S.C.M., T.F.J., M.C., and F.A.-P.); the US DOE Office of Science under contract no. DE-AC02-05CH11231 (S.C.M. and F.A.-P.); the DOE Office of Science, National Energy Research Scientific Computing Center (NERSC) under BES-ERCAP0024127 (S.C.M. and F.A.-P.); and the DOE Office of Science, SLAC Scientific Data Facility (SDF) (S.C.M. and F.A.-P.). **Author contributions:** Conceptualization: C.K.S.; Funding acquisition: J.P., M.C., F.A.-P.; Investigation: C.K.S., J.J., S.C.M., S.K., H.K., T.Y.K., You.K., K.R.L., J.S.K., C.K., G.J.; Methodology: C.K.S., J.J.; Project administration: J.P.; Supervision: J.P.; Visualization: C.K.S., J.P.; Writing – original draft: C.K.S., S.C.M., J.P.; Writing – review & editing: C.K.S., S.C.M., J.J., C.K., J.C., Yon.K., C.W.Y., T.F.J., F.A.-P., M.C., J.P. **Competing interests:** The authors declare that they have no competing interests. **Data, code, and materials availability:** All data and details of materials synthesis are available in the main text or the supplementary materials. The spreadsheet source data underlying the plots in the main text and supplementary materials are available through Zenodo (*57*). DFT-optimized structures, energies, and related metadata are available at Catalysis-Hub (https://www.catalysis-hub.org/publications/SongStrongly2026.db). **License information:** Copyright © 2026 the authors, some rights reserved; exclusive licensee American Association for the Advancement of Science. No claim to original US government works. https://www.science.org/about/science-licenses-journal-article-reuse

SUPPLEMENTARY MATERIALS

science.org/doi/10.1126/science.aeb3087
Materials and Methods; Figs. S1 to S38; Tables S1 to S3; References (*58*–*84*)

Submitted 9 August 2025; resubmitted 2 December 2025; accepted 8 April 2026

10.1126/science.aeb3087

Downloaded from https://www.science.org at University of Bath on October 27, 2026

Science
AAAS

Dependence of catalytic properties of strongly supported platinum clusters with atom counts

Chyan Kyung Song, Junhyeok Jung, Shyama Charan Mandal, Sungsu Kang, Tae Yong Kim, Chan Kim, Gyeongrok Jang, Hyungjoo Kim, Younhwa Kim, Kyung Rok Lee, Ji Soo Kim, Junjie Chen, Yongmin Kim, Chang Won Yoon, Thomas F. Jaramillo, Matteo Cargnello, Frank Abild-Pedersen, and Jungwon Park

Science **392** (6801), . DOI: 10.1126/science.aeb3087

Editor's summary

Song *et al*. created strongly anchored clusters of platinum on alumina by reducing $PtCl_42\#$ with methanol. They then used electron microscopy to show that clusters with the same 1-nanometer diameter could vary in total atom count by a factor of three. X-ray absorption spectroscopy showed that clusters with higher atom counts had stronger interactions with the support. For hydrogen production from cyclic hydrocarbons, clusters with fewer atoms had higher activity, but those with more atoms were more durable and selective. —Phil Szuromi

View the article online
https://www.science.org/doi/10.1126/science.aeb3087
Permissions
https://www.science.org/help/reprints-and-permissions

Use of this article is subject to the Terms of service

Science (ISSN 1095-9203) is published by the American Association for the Advancement of Science. 1200 New York Avenue NW, Washington, DC 20005. The title *Science* is a registered trademark of AAAS.

Copyright © 2026 The Authors, some rights reserved; exclusive licensee American Association for the Advancement of Science. No claim to original U.S. Government Works

Downloaded from https://www.science.org at University of Bath on October 27, 2026